AGU PUBLICATIONS

JGR

Journal of Geophysical Research: Atmospheres

RESEARCH ARTICLE

10.1002/2014JD022643

Key Points:
- Total cloud cover from various methods is in 65–85% within ±1 okta
- Sky camera overestimates cloudiness with respect to other automatic methods
- Clouds can be correctly classified in 50–90% of cases using sky cameras

Supporting Information:
- Figure S1
- Movie S1

Correspondence to:
S. Wacker,
stefan.wacker@pmodwrc.ch

Citation:
Wacker, S., J. Gröbner, C. Zysset, L. Diener, P. Tzoumanikas, A. Kazantzidis, L. Vuilleumier, R. Stöckli, S. Nyeki, and N. Kämpfer (2015), Cloud observations in Switzerland using hemispherical sky cameras, *J. Geophys. Res. Atmos.*, *120*, 695–707, doi:10.1002/2014JD022643.

Received 29 SEP 2014
Accepted 1 JAN 2015
Accepted article online 7 JAN 2015
Published online 30 JAN 2015

Cloud observations in Switzerland using hemispherical sky cameras

Stefan Wacker[1,2], Julian Gröbner[1], Christoph Zysset[1,3], Laurin Diener[1], Panagiotis Tzoumanikas[4], Andreas Kazantzidis[4], Laurent Vuilleumier[5], Reto Stöckli[6], Stephan Nyeki[1], and Niklaus Kämpfer[7]

[1]Physikalisch-Meteorologisches Observatorium Davos, Davos Dorf, Switzerland, [2]Now at Asiaq, Nuuk, Greenland, [3]Now at Computer Controls AG, Otelfingen, Switzerland, [4]Laboratory of Atmospheric Physics, University of Patras, Patras, Greece, [5]Federal Office of Meteorology and Climatology MeteoSwiss, Payerne, Switzerland, [6]Federal Office of Meteorology and Climatology MeteoSwiss, Zürich-Flughafen, Switzerland, [7]Institute of Applied Physics, University of Bern, Bern, Switzerland

Abstract We present observations of total cloud cover and cloud type classification results from a sky camera network comprising four stations in Switzerland. In a comprehensive intercomparison study, records of total cloud cover from the sky camera, long-wave radiation observations, Meteosat, ceilometer, and visual observations were compared. Total cloud cover from the sky camera was in 65–85% of cases within ±1 okta with respect to the other methods. The sky camera overestimates cloudiness with respect to the other automatic techniques on average by up to 1.1 ± 2.8 oktas but underestimates it by 0.8 ± 1.9 oktas compared to the human observer. However, the bias depends on the cloudiness and therefore needs to be considered when records from various observational techniques are being homogenized. Cloud type classification was conducted using the *k*-Nearest Neighbor classifier in combination with a set of color and textural features. In addition, a radiative feature was introduced which improved the discrimination by up to 10%. The performance of the algorithm mainly depends on the atmospheric conditions, site-specific characteristics, the randomness of the selected images, and possible visual misclassifications: The mean success rate was 80–90% when the image only contained a single cloud class but dropped to 50–70% if the test images were completely randomly selected and multiple cloud classes occurred in the images.

1. Introduction

Clouds are the principal modulator of the Earth's radiation budget by reflecting solar radiation back to space and by trapping and reemitting long-wave (thermal) radiation emitted by the surface and the lower troposphere. Clouds remain the largest uncertainty in the estimates and interpretation of the Earth's changing radiation budget [*Boucher et al.*, 2013]. Problems include among others the lack of global and quantitative surface measurements, many different kinds of inhomogeneities in the data sets, and insufficient precision to measure the small changes in cloudiness that nevertheless can have large impacts on Earth's climate [e.g., *Norris and Slingo*, 2009]. Most of these deficiencies are due to the absence of observing systems designed to monitor cloudiness and its variations with high precision. Therefore, it is crucial to establish such observing systems which allow cloudiness and its variations to be accurately monitored.

Cloudiness has been observed worldwide for decades by human observers. These records are undoubtedly the most important archive to study long-term changes in cloudiness. However, this observation technique is being increasingly replaced by automatic methods, mostly due to economical pressure. The replacements have often caused substantial inhomogeneities in these important records [*Dai et al.*, 2006]. Besides their costs, the relatively low temporal resolution of human cloud observations—in contrast to the highly dynamical cloud system—show their limitation and the need for automatic ground-based systems. Automatic ground-based techniques include devices such as the ceilometer, cloud radar, long-wave radiometers, pyrradiometers, and hemispherical sky cameras [*Boers et al.*, 2010].

In recent years, the use of hemispherical sky cameras has been steadily increasing. While the first camera systems, a series of Whole Sky Imagers developed by the Scripps Institution of Oceanography at the University of California [e.g., *Johnson et al.*, 1989; *Shields et al.*, 2003, 2013] and the commercially distributed Total Sky imager [*Long and DeLuisi*, 1998], were relatively expensive due to the high-quality optics and engineering involved, the rapid development of low-cost digital cameras has favored their application for

cloud observations. Numerous research groups nowadays use various camera systems developed for their specific needs [e.g., *Feister and Shields*, 2005; *Kalisch and Macke*, 2008; *Kreuter et al.*, 2009].

Cloud detection and the calculation of total cloud cover are based on algorithms which use the red-green-blue (RGB) image in combination with a camera-dependent threshold to discriminate between cloud-free and cloudy pixels. Various ratios and/or differences of the three-color channels for cloud detection have been discussed and are in use [e.g., *Long et al.*, 2006; *Heinle et al.*, 2010; *Ghonima et al.*, 2012; *Kazantzidis et al.*, 2012]. Hemispherical sky cameras are a powerful alternative to commonly used cloud observation techniques because of (1) temporally high-resolved observations and (2) imaging of the total hemisphere on a pixel basis yielding total cover in percentage coverage of the sky. Some of the deficiencies include the hampered detection of cloudy pixels near the Sun and the limitation of the method to daytime observations for most of the systems in use. An exception is the DayNight Whole Sky imager with its high dynamic range and sensitivity which allows night time images to be acquired and processed [*Shields et al.*, 2013].

Besides total cloud cover, the camera systems allow the clouds to be classified into different cloud classes using statistical methods. Cloud type classification is an essential requirement to study the effect of various cloud types on the radiative processes in the atmosphere and on the surface radiation budget in order to minimize uncertainties. However, cloud type observations have so far been mainly restricted to human observers and no automatic technique is available on an operational basis. The concept of cloud type classification using hemispherical sky cameras is based on a nonparametric classifier which discriminates clouds using various characteristics which describe the spectral and textural properties of clouds [e.g., *Heinle et al.*, 2010; *Kazantzidis et al.*, 2012]. It was found that clouds can be correctly classified in 75–95% of cases. Finally, sky cameras are beginning to be used for intrahour and subkilometer cloud forecasting and solar irradiance nowcasting [*Quesada-Ruiz et al.*, 2014; *Yang et al.*, 2014]. This broad range of applications demonstrates the potential of such camera systems in meteorology and climate sciences.

We have established a camera network in Switzerland to observe total cloud cover and to conduct cloud type classification. We will present the first results and compare the observations of total cloud cover to corresponding observations from other techniques. In section 2, the network and methods are described. Section 3 presents the results and includes a comparison of total cloud cover calculated using two different sky camera algorithms (section 3.1), intercomparisons of total cloud cover derived from various techniques (section 3.2), and cloud type classification at all sites (section 3.3). The results are discussed in section 4. Finally, concluding remarks and a brief outlook are given in section 5.

2. Data and Methods

2.1. Camera Network and Hardware

Hemispherical sky cameras have been installed at four sites in Switzerland (see Table 1). In 2010, a camera system was deployed at the Physikalisch-Meteorologisches Observatorium Davos/World Radiation Center (PMOD/WRC) in Davos. In 2011, a camera was installed at Payerne, which is a station of the Global Climate Observing System Reference Upper Air Network and the Baseline Surface Radiation Network (BSRN). Previous to this, a camera system had also been installed at Zimmerwald observatory, operated by the Astronomical Institute and the Institute of Applied Physics of the University of Bern. However, due to technical problems with the camera system in combination with the remoteness of the site, this camera was only occasionally in operation and the use of its data is limited to cloud type classification in this study. Finally, the last camera was deployed in 2012 at the high alpine and Global Atmospheric Watch site Jungfraujoch. All sites are collocated with ancillary observations of various atmospheric parameters used in this study such as screen level temperature, downwelling long-wave radiation (DLR), and integrated water vapor. In addition, ceilometer data are available at Payerne and Zimmerwald, and visual cloud observations at Payerne and Jungfraujoch.

Cloud observations began at Davos, Zimmerwald, and Payerne with a CMS (Schreder GmbH) camera system (www.schreder-cms.com/) which consists of a commercial Canon digital camera (Canon Power Shot A60) with a fish eye lens enclosed by a glass dome to protect the optics from the environment. Pictures are acquired every 5 min and have a resolution of 1200 × 1600 pixels. A second underexposed picture (1/1600 s exposure) is taken just after the first which has an exposure at 1/500 s (normal exposed picture). Pictures are taken at a fixed aperture $f/8$. The underexposed picture is used to determine whether the Sun is covered

Table 1. Station Names, Coordinates, Altitude, and Date of Installation of the Sky Cameras

Station	Coordinates	Altitude (masl)	Camera Type	Begin of Operation[a]
Payerne (PAY)	46.81°N, 6.94°E	490	Schreder	25/3/2011
Zimmerwald (ZIM)	46.87°N, 7.47°E	907	Schreder	30/8/2010
Davos (DAV)	46.81°N, 9.84°E	1610	Schreder/MOBOTIX	27/3/2010
Jungfraujoch (JFJ)	46.55°N, 7.98°E	3584	MOBOTIX	25/7/2012

[a]Dates are formatted as day/month/year.

by clouds or not. If the Sun is not covered by clouds, the underexposed picture is also used to reliably evaluate the image and to detect those pixels, which are often saturated due to the Sun's high intensity. Due to frequent failures particularly during very cold weather conditions, a more robust system was acquired for Davos and Jungfraujoch. A commercial surveillance camera from MOBOTIX (www.mobotix.com) was chosen which includes a high-resolution 3 megapixel color sensor with a fish eye lens. Pictures are taken every minute at an exposure of 1/500 s and have a 1200 × 1600 pixel resolution. The camera in Davos was installed in April 2013 in a ventilation unit on a solar tracker with shading disks to impede the formation of ice and snow on the lens and to permanently block the direct beam of the Sun. The same setup was used at Jungfraujoch, but the camera was not installed on a solar tracker, as it was the case at Payerne and Zimmerwald.

The MOBOTIX system has not been designed for climate applications while the quality of the optics is considerably lower compared to the Schreder system. However, the MOBOTIX system is more robust regarding operation under harsh environmental conditions. The pictures of the MOBOTIX were only used for Jungfraujoch in this study.

2.2. Cloud Detection and Calculation of Total Cloud Cover

2.2.1. Hemispherical Sky Camera

Image processing algorithms calculate total cloud cover by determining whether a cloud is present in each pixel using the measured color in combination with a reference value. Before the color criteria can be applied to the images, they need to be preprocessed. Since the horizon at Davos and Jungfraujoch is characterized by high mountain ridges, the images need to be masked in order to evaluate only the relevant pixels of the sky. The flat horizon at Payerne and Zimmerwald is cut at a constant angle of 12° to remove buildings and trees near the horizon.

A color mask is generated out of the (normal exposed) RGB color signal using the ratios of the blue to the green channel and the blue to the red channel for each pixel. The color mask is then compared to a reference value to generate a blue and a cloudy sky mask of the normal exposed image. The reference value is set to 2.5 for the Schreder camera while for the MOBOTIX a value in the range 1.82–2.2 is used depending on the image settings. If the corresponding value of the pixel is greater than the reference value the pixel is interpreted as blue, otherwise it is interpreted as cloudy. For the Schreder system, the underexposed image is also used for a precise cloud detection if the Sun is not covered by clouds resulting in brighter pixels. A single simplified image is obtained by adding the blue sky and cloudy sky masks of the normal and underexposed image. In this resulting image, cloudy, cloud-free, and "Sun" pixels are represented by white, blue, and red colors, respectively (see Figure 1). The total cloud cover is then calculated as the ratio of the total number of white pixels to the total number of relevant pixels in the processed image.

We will refer to the image processing algorithm and the cloud type classification algorithm which will be described in section 2.3 as the "PMOD-algorithm." Total cloud cover and cloud type classification from the PMOD-algorithm will also be compared to the corresponding outputs from a different image processing algorithm, the "sky analyzer." The sky analyzer was developed by the University of Patras [*Kazantzidis et al.*, 2012]. It uses a combination of the red, blue, and green channels with three distinct thresholds to calculate total cloud cover. According to results, the multicolor criterion outperforms methods that are based on the ratio or the difference of the red and blue channels for cases of broken or overcast cloudiness under large solar zenith angles. The comparison of the total cloud coverage values, derived from the proposed method with SYNOP observations at a nearby airport at Thessaloniki, Greece, showed that 83% and 94% of the analyzed images agreed to within ±1 and ±2 oktas, respectively. These images were acquired using a commercial compact digital camera (Canon IXUS II).

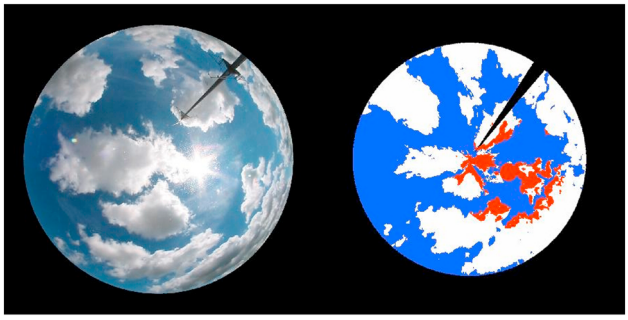

Figure 1. (left) Original and (right) processed image of the sky over Payerne on the 22 May 2012 12:40 UTC. The processed image has been rectified. The Sun mask and saturated pixels outside the mask are colored in red. The calculated total cloud cover is 48% for this image.

2.2.2. Visual Cloud Observations

Visual observations of total cloud cover are the longest records of cloudiness and therefore of great importance for long-term analysis. The method is simple: A trained observer looks at the sky and estimates the total cloud cover in oktas following the WMO guidelines. Visual cloud observations are conducted around 6, 9, 12, 18, 21, and 24 UTC, and around 6, 9, 12, 15, and 18 UTC at Payerne and Jungfraujoch, respectively. A visual observation period at MeteoSwiss covers 15 min from xx:30 to xx:45 before the official WMO observation hours. During this period the observations can be updated and revised.

2.2.3. Observations of Long-Wave Radiation

Observations of downwelling long-wave radiation (DLR) can be used to detect clouds and calculate total cloud cover during day and night. The Automatic Partial Cloud Amount Detection Algorithm (APCADA) uses downwelling long-wave radiation, its variability, air temperature, and relative humidity at screen level height in combination with a set of empirical rules to detect clouds and calculate total cloud cover [*Dürr and Philipona*, 2004]. In principle, the apparent emittance of the sky is calculated from screen level temperature and measured long-wave radiation using the Stefan-Boltzmann law and compared to a calculated apparent cloud-free emittance. If the ratio of the apparent emittance to the empirical cloud-free emittance is smaller or equal to 1, the sky is cloud free; otherwise it is cloudy. This ratio is then used in combination with the standard deviation of DLR calculated over the past 60 min and a set of empirical rules to determine total cloud cover at a 10 min resolution.

Observations of DLR are conducted at all four sites following Baseline Surface Radiation Network (BSRN) guidelines. BSRN is dedicated to observe the surface radiative fluxes at a small number of sites in contrasting climatic zones with instruments of the highest available accuracy and with high temporal resolution, i.e., 1 to 3 min [*Ohmura et al.*, 1998]. We use high precision instruments such as the Eppley PIR pyrgeometer and the CG(R)4 pyrgeometer from Kipp&Zonen at all four sites. The DLR is measured every 10 s, and 1 min averages are recorded. All pyrgeometers are operated in a ventilation unit including a copper heating ring to continuously blow slightly preheated air over the pyrgeometer domes. This setup impedes the formation and accumulation of thaw, rime, ice, and snow on the instrument domes.

2.2.4. Meteosat

The geostationary Meteosat satellites of the Second Generation (MSG = Meteosat 8–10) are located directly over the equator at a longitude of 0° and at an altitude of about 36,000 km. MSG carries a radiometer that measures in 12 different spectral bands in the visible and infrared (SEVIRI; Spinning Enhanced Visible and InfraRed Imager) at a horizontal resolution of around 3 km (3.2 × 5.5 km over Switzerland) every 15 min. In addition, there is a high-resolution visible (HRV) channel with a spatial resolution of around 1 km (1.1 × 1.8 km over Switzerland).

MeteoSwiss is currently developing a cloud mask algorithm for the determination of cloud amount from MSG. The cloud mask algorithm is based on continuous cloudiness scores instead of the traditional binary decision tree approach which is used in most applications. The scores are calculated for different channels as well as for different spatial and temporal statistical quantities. Each score yields a probability for the pixel's cloud cover. The final result, the cloud cover probability, is obtained by summing up all available scores, taking into account the varying performance of the scores during day and night and over snow. The most important advantage of this approach over the decision tree method is that incorrectly assigned pixels within the tree, and thus subsequent tests following the wrong branch, can be avoided. Thus, the cloud mask calculated using scores is more cloud or cloud-free conservative. Unlike most cloud masks depending on clear sky temperature from weather models or coarse climatologies of cloud-free albedo, the cloud mask builds its own cloud-free background data over time from cloud-screened reflectances and brightness

Table 2. Conversion Table From Cloudiness Denoted as Percentage for the Sky Camera and Meteosat, and the Number of Hits Divided by the Total Number of Possible Hits *n* for the Ceilometer

Percent	*n*	Okta
Percent ≤ 5	$n \leq 0.0625$	0
$5 \leq \% < 18.75$	$0.0625 \leq n < 18.75$	1
$18.75 \leq \% < 31.25$	$0.1875 \leq n < 0.3123$	2
$31.25 \leq \% < 43.75$	$0.3123 \leq n < 0.4375$	3
$43.75 \leq \% < 56.25$	$0.4375 \leq n < 0.5625$	4
$56.25 \leq \% < 68.75$	$0.5625 \leq n < 0.6875$	5
$68.75 \leq \% < 81.25$	$0.6875 \leq n < 0.8125$	6
$81.25 \leq \% < 95$	$0.8125 \leq n < 0.9375$	7
Percent ≥ 95	$n \geq 0.9375$	8

temperatures. This renders the cloud mask independent of external (nonsatellite) data sets. Furthermore, it is not necessary that all scores are available, as a subset is sufficient to obtain a final aggregated rating [*Stöckli*, 2013].

For this intercomparison, a cloudiness for the year 2012 has been processed using the new algorithm. The parameters have been derived for a subgrid of 10×10 pixels from the SEVIRI HRV channel (resolution is approximately 1×1.5 km per pixel) with Payerne at the grid center. Total cloud cover (TCC) is calculated as the fraction of the sum of completely overcast pixels and partly cloudy pixels over the total number of pixels:

$$\mathrm{TCC} = \frac{\sum \text{overcast} + f \sum \text{partly cloudy}}{\sum \text{all pixels}}, \quad (1)$$

The partly cloudy pixels are multiplied by a factor *f* in order to correct for the fact that broken clouds do not completely fill the satellite's field of view. For this study we took a value of 0.75 which was derived from a validation study of MSG/SEVIRI data using synoptical stations [*Karlson et al.*, 2005].

2.2.5. Ceilometer

The ceilometer used in Payerne is a CBME80 ceilometer from Eliasson. The CBME80 ceilometer measures cloud height or vertical visibility (if no clouds are present) up to 7500 m, with a resolution of 10 m, and is able to detect up to four cloud layers. The cloud amount algorithm is an enhanced version of the algorithm developed by the National Weather Service in the U.S. [e.g., *National Oceanic and Atmospheric Administration*, 1998]. A detailed description of the algorithm can be found in the User's Guide of the CBME80 [*Eliasson*, 2005]. Backscatter return signals are sampled every 30 s and the height of possible cloud "hits" is determined. In addition, fractional and total cloud covers are calculated every 30 s using the last 30 min of 30 s data. Thereby, the last 10 min have a double weighting to be more responsive to the latest changes in sky conditions. As a consequence, a value of total cloud cover is calculated every 30 s from a 30 min interval which includes a total of 80 samples. It is calculated as the number of hits during the 30 min time interval divided by the number of possible hits, i.e., 80. The scheme to convert the vertically detected cloud layers to cloudiness in oktas is denoted in Table 2.

2.2.6. Definition of Total Cloud Cover and Averaging Procedure

In order to compare cloudiness from various techniques the same units of measurement should be used. Cloudiness is reported as a percentage for sky camera and Meteosat data, while APCADA and the Ceilometer report cloudiness in okta units. Cloudiness in percentage was therefore converted into okta. According to the WMO guidelines, the values of 0 and 8 okta correspond to completely cloud-free (0%) and completely cloudy conditions (100%). We used a slightly modified conversion scheme which allows total cloud cover up to 5 and over 95% to be within the 0 and 8 okta bins, respectively (see Table 2). This implies that the 0, 1, 7, and 8 okta bins are associated with different ranges (namely, 5 and 13.75%) of total cloudiness conditions rather than the intermediate range (12.5%). Furthermore, no cloud-free cases and only a few overcast situations would be detected by the sky camera if the WMO definition was used. Note that the ceilometer algorithm also uses a slightly different conversion scheme to convert the vertical layers to hemispherical oktas. Cloud hits are also possible in the 0 okta bin as well as the 8 okta bin which does not necessarily have to be for an overcast sky.

Visual observations are recorded during a 15 min period. To compare the visual cloud observations with the sky camera data, we averaged total cloud cover from the images acquired during this 15 min period. The output from the various automatic instruments is available at different time resolutions. While the cloud cover from the ceilometer at Payerne has a time resolution of 30 s (but derived from the past 30 min of the respective sample), cloudiness from the sky camera is available at 5 min intervals. Observations of the downwelling long-wave radiation are taken every minute. The long-wave observations are averaged to

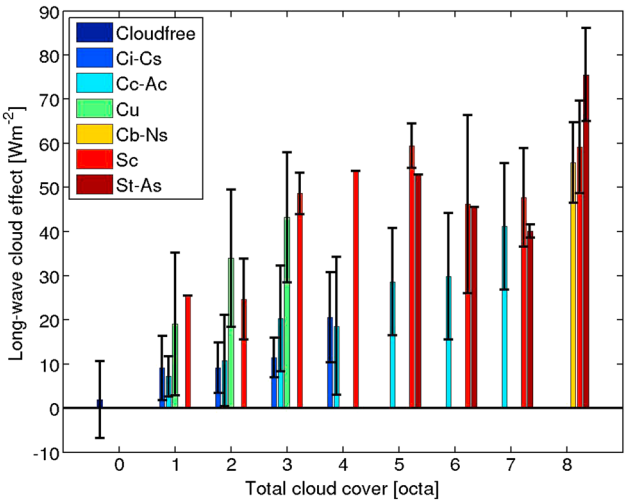

Figure 2. Long-wave cloud effect as a function of total cloud cover for six cloud classes and cloud-free conditions at Payerne. The bars represent 1 standard deviation. Total number of observations is 1346.

10 min bins to be consistent with the observations of instantaneous screen level temperature and relative humidity which are then used for the calculation of total cloud cover using APCADA. A Meteosat scan takes about 15 min and starts at the South Pole. The actual scanning time over Payerne is 4 min before each quarter hour. Therefore, we took the MSG slots at xx:11 and xx:41 and compared the outputs to the corresponding outputs of the other methods. For the intercomparison at Davos where only sky camera and APCADA data are available we used the values at the full and half hour in order to obtain an independent data set.

2.3. Cloud Type Classification

Besides the calculation of total cloud cover, we have adopted and tested the algorithm of *Heinle et al.* [2010] to classify the images into seven different cloud classes: cirrus-cirrostratus (ci-cs), cirrocumulus-altocumulus (cc-ac), stratus-altostratus (st-as), cumulus (cu), stratocumulus (sc), cumulonimbus-nimbostratus (cb-ns), and cloud free (cf). The cloud type classification algorithm is based on a set of statistical features describing the color (spectral features) and the texture of an image (textural features). *Heinle et al.* [2010] proposed 12 features for application after extensively testing numerous features. The spectral features include the mean of the red and blue channels, standard deviation and skewness of the blue channel, and the differences between the red and green, red and blue, and green and blue channels. The textural features include the energy, entropy, contrast, and homogeneity of the blue channel. Furthermore, the total cloud cover is used as an additional feature. We have adopted all these features except the entropy which is—in our opinion—not helpful because the values of the various cloud classes interfere significantly with each other and, therefore, its use for discrimination is limited.

In addition, we introduced a radiative feature which is based on the long-wave radiation: the "long-wave cloud effect" (LCE) which describes the radiative effect of clouds on long-wave radiation. We calculate the long-wave cloud effect as the difference between the measured long-wave radiation (during cloudy conditions) and the long-wave flux that would be expected at the same time in the absence of the clouds assuming the same vertical temperature and humidity distribution as for the cloudy case. The cloud-free flux is calculated using a cloud-free model which accounts for the temperature lapse rate in the atmospheric boundary layer [*Gröbner et al.*, 2009; *Wacker et al.*, 2014]. The LCE depends among others on the cloud type (cloud base temperature) and fractional cloud cover. It is smaller for high-level clouds due to their weak radiative impact on the surface long-wave radiation compared to low-level clouds which have a larger radiative impact and thus a larger long-wave cloud effect (see Figure 2). The cloud class "stratus-altostratus" yields the highest mean LCE at 75.3 ± 11.5 Wm^{-2} during overcast conditions and is dominated by the cloud type stratus nebulosus (fog) which frequently occurs from October to April at Payerne.

The mean success rate of the cloud type classification algorithm was 1.6, 5.5, and 10.8% higher (averaged over all seasons) at Payerne, Zimmerwald, and Davos, respectively, when using this radiative feature. All cloud classes were better recognized except stratus-altostratus and cumulonimbus-nimbostratus. For these two cloud classes the success rate was even lower, probably due to their similar LCE. The overall performance of the algorithm at Jungfraujoch was not better most likely due to the higher uncertainties of the long-wave observations and the corresponding cloud-free model [*Wacker et al.*, 2014].

For the actual classification of an image, the *k*-Nearest Neighbor (*k*NN) classifier is used. The *k*NN method belongs to the "supervised," nonparametric classifiers. "Supervised" implies that the separating classes are known and a training set is used to train the algorithm. We generated such a training sample from the Payerne data set by visual inspection of the images. This data set was chosen to train the algorithm because

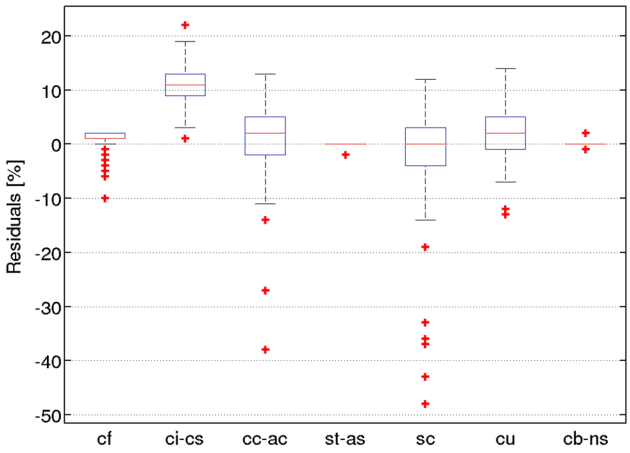

Figure 3. Difference in cloud cover between the PMOD and the sky analyzer algorithms for various cloud classes. The cloud classes are cloud free (cf), cirrus-cirrostratus (ci-cs), cirrocumulus-altocumulus (cc-ac), stratus-altostratus (st-as), cumulus (cu), stratocumulus (sc), and cumulonimbus-nimbostratus (cb-ns). The red line in the boxes represents the median of the differences. Red crosses are outliers which are larger than $q3+1.5(q3-q1)$ or smaller than $q1-1.5(q3-q1)$, where $q1$ and $q3$ are the 25th and 75th percentiles represented by the lower and upper edge of the boxes, respectively. Total number of observations is 480.

a large number of ancillary data including synoptic observations and ceilometer data have facilitated the generation of the training set. In order to train the algorithm, the images of the training set contain only one single cloud class as previously defined. The training set contains about 200 pictures for each cloud class for which the 12 features were calculated and stored with the assigned cloud class. The actual classification of a test image is conducted by calculating the distance between the feature vector of the test image and the feature vectors of each element in the training set. The class of the test image is then determined based on the majority vote of the k closest neighbor classes. If the majority vote is not unique, the class of the closest element in the training set determines the class of the test image. We used $k = 3$.

In order to study the performance of the algorithm at the other three stations and for images which do not necessarily show one unique cloud class as the Payerne training sample does, we generated independent test samples for the four sites. The Matlab function "randi" was used to randomly select single images from the whole data set. The test sets contained 163, 184, 195, and 204 images for Zimmerwald, Payerne, Jungfraujoch, and Davos, respectively. The selected images were visually and independently classified by two observers, and the 12 features were calculated and stored with the assigned cloud class. If clouds from more than one cloud class occurred simultaneously in the image, the image was visually classified according to the predominant cloud class.

The sky analyzer was also used to classify the images from the Payerne sets. Besides total cloud cover, the sky analyzer uses the same seven color and three textural features as the PMOD-algorithm. In addition, a metric which describes the existence of raindrops on the glass dome is included in the algorithm [*Kazantzidis et al.*, 2012]. Furthermore, a number of subclasses are created for every cloud class, based on parameters that have a large effect on the distribution of light in the sky, namely, the solar zenith angle, the cloud coverage, and the visible fraction of the solar disk. This is because clouds belonging to the same type under different atmospheric conditions may vary substantially when the metrics for classification are considered.

3. Results

3.1. Total Cloud Cover From Two Different Image Processing Algorithms

A data set comprising 480 images from Payerne was selected to compare the PMOD and sky analyzer algorithms. The images were visually screened and include the occurrence of a single cloud type only. The definition of cloud types is identical to that used for cloud classification discussed in section 2.3.

The relative mean difference in cloudiness between the two algorithms was $1.0 \pm 7.6\%$ (1 standard deviation). The results differ substantially among the individual cloud types (see Figure 3): Although the results for cloud-free, stratus-altostratus, and cumulonimbus-nimbostratus yielded good agreement because most of these events are related to cloudiness of 0 and 100%, respectively (or close to these values), the discrepancies between the two algorithms were larger for the remaining cloud classes. While the median of the differences for cirrocumulus-altocumulus, stratocumulus, and cumulus remained small and about 99% of the images were within $\pm 10\%$ (as represented by the range enclosed by the whiskers), the median of the differences was substantially larger for cirrus-cirrostratus at 10%.

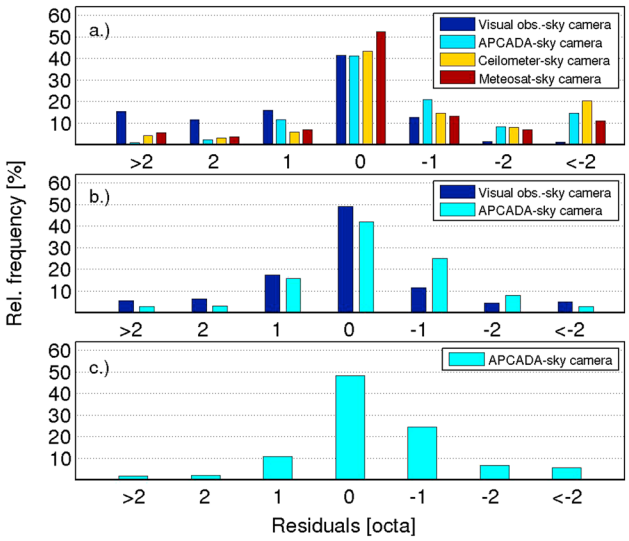

Figure 4. Relative frequency of total cloud cover differences between various techniques at (a) Payerne, (b) Jungfraujoch, and (c) Davos. Total number of compared outputs for Payerne is 2853, 7714, 6723, and 7947 for the sky camera-human observer, sky camera-APCADA, sky camera-ceilometer, and sky camera-Meteosat intercomparison, respectively. The data set from Jungfraujoch contains 1334 and 1293 observations for the sky camera-human observer and sky camera-APCADA intercomparison, respectively. For the Davos intercomparison, 5806 outputs from the sky camera and from APCADA have been compared.

3.2. Total Cloud Cover From Different Observational Techniques

For the intercomparison of various automatic methods at the Payerne site a data set covering all seasons in 2012 was used. The data set comprises simultaneous observations of total cloud cover derived from the sky camera using the PMOD-algorithm, APCADA, ceilometer, and Meteosat. In order to increase the number of visual observations to be compared to the sky camera, a data set covering a longer period (2011–2014) was produced. For all intercomparisons at the Payerne site, the Schreder system was used.

The sky camera frequently underestimates total cloud cover with respect to the observer. Indeed, in 43% of all cases the sky camera calculated a lower cloudiness as shown by the frequency distribution of the residuals in Figure 4 which has a clear asymmetric shape. In 41% of cases the two methods reported the same cloudiness. The outputs were in 70 (84)% of cases within ±1 (2) oktas, and thus, in 16% of all cases the difference was larger than ±2 oktas.

Compared to the automatic methods, however, the sky camera tends to overestimate cloudiness. While in the sky camera-APCADA and sky camera-ceilometer comparison the sky camera calculated in 44% of cases a higher total cloud cover, this fraction was substantially lower in the sky camera-Meteosat comparison at 31%.

The sky camera data showed the best agreement with Meteosat. In 52% of all cases these two techniques calculated the same cloudiness, while in the sky camera-APCADA and sky-camera-ceilometer comparison 41 and 43% of the outputs were consistent, respectively. Results from the sky camera-ceilometer, sky camera-Meteosat, and sky-camera-APCADA intercomparisons were in 64 (75), 72 (84), and 74 (84)% of cases within ±1 (2) oktas, respectively. Outputs from the sky camera and the ceilometer differed in 24% of cases by more than ±2 oktas and hence showed the worst agreement, while this fraction was substantially lower in the other two intercomparisons at 16–17%.

Observations from Jungfraujoch and Davos yielded similar results. For Jungfraujoch a 1 year data record from the MOBOTIX camera was used (2012/2013). As in Payerne, the sky camera calculated lower values of total cloud cover more frequently with respect to the observer but higher values compared to APCADA. Consistency was better between the sky camera and the observer, namely, 49% of the outputs yielded the same cloudiness and 78 (89)% were within ±1 (2) okta. In the sky camera-APCADA intercomparison 42% of the observations were consistent and 83 (94)% were within ±1 (2) okta. These results indicate that the camera type may not have a notable impact on the results at least in the coarse okta measuring system.

A data record going back to 2010 was available at Davos. Note that only pictures acquired with the Schreder system were used for this intercomparison. The comparison between the sky camera and APCADA was slightly more consistent compared to Payerne and Jungfraujoch, probably due to the larger data set. In 48% of all cases the two methods yielded the same cloudiness and 84 (92)% of the observations were within ±1 (2) okta. APCADA underestimated the total cloud cover also at Davos compared to the sky camera. Indeed, in 70% of the outputs which yielded a different okta value, APCADA calculated a lower total cloud cover. The underestimation is probably mainly caused by cirrus clouds which cannot be detected

Table 3. Contingency Matrix for the Payerne Training Set and the Manually Created Payerne Test Set[a]

True Class	Classified as: cf TS	cf TEST	ci-cs TS	ci-cs TEST	cc-ac TS	cc-ac TEST	st-as TS	st-as TEST	sc TS	sc TEST	cu TS	cu TEST	cb-ns TS	cb-ns TEST	Mean Success rate TS	Mean Success rate TEST
cf	**96.7**	**92.5** (**97.5**)	3.3	5.0 (2.5)	0.0	2.5 (0.0)	0.0	0.0 (0.0)	0.0	0.0 (0.0)	0.0	0.0 (0.0)	0.0	0.0 (0.0)		
ci-cs	0.0	6.0 (8.0)	**98.5**	**84.0** (**82.0**)	1.5	2.0 (6.0)	0.0	2.0 (0.0)	0.0	0.0 (2.0)	0.0	6.0 (2.0)	0.0	0.0 (0.0)		
cc-ac	0.7	0.0 (0.0)	0.7	10.4 (8.3)	**71.4**	**72.9** (**79.2**)	0.7	0.0 (0.0)	10.0	4.2 (2.1)	15.7	10.4 (10.4)	0.7	2.1 (0.0)		
st-as	0.0	0.0 (0.0)	0.0	0.0 (0.0)	0.8	0.0 (10.0)	**94.7**	**96.7** (**53.3**)	2.9	3.3 (0.0)	0.0	0.0 (0.0)	1.6	0.0 (36.7)		
sc	0.0	0.0 (0.0)	0.0	0.0 (0.0)	1.1	3.9 (10.0)	3.7	11.8 (4.0)	**93.7**	**47.1** (**70.0**)	0.0	25.5 (4.0)	1.6	11.8 (12.0)		
cu	0.6	0.0 (2.0)	0.0	2.0 (2.0)	7.6	2.0 (5.9)	0.6	0.0 (0.0)	0.6	0.0 (0.0)	**90.0**	**96.1** (**90.2**)	0.6	0.0 (0.0)		
cb-ns	0.0	0.0 (0.0)	0.0	0.0 (0.0)	0.0	0.0 (0.0)	5.7	17.6 (0.0)	2.6	7.8 (0.0)	1.8	5.9 (0.0)	**89.9**	**68.6** (**100.0**)	**91.7**	**78.2** (**83.1**)

[a]Shown are the relative frequencies in percent of the PMOD-algorithm for the Payerne training set (TS) using the Leave-One-Out Cross-Validation (LOOCV) and for the test set (TEST). In addition, the corresponding results from the sky analyzer for TEST are given in parentheses. The cloud classes are cirrus-cirrostratus (ci-cs), cirrocumulus-altocumulus (cc-ac), stratus-altostratus (st-as), cumulus (cu), stratocumulus (sc), cumulonimbus-nimbostratus (cb-ns), and cloud free (cf). Highlighted in bold are the percentages of correctly classified cases in the respective cloud class. The test set contains total 321 images.

by APCADA due to their weak signal in the long wave measured at the surface while their radiative effect in the short wave (and hence in the signal detected by the sky camera) is considerably larger. In fact, sky camera algorithms for the detection of optical thin cirrus clouds have been developed [e.g., *Shields et al.*, 1990]. In contrast, the reliable use of APCADA is limited to cloud detection of low level and midlevel clouds [*Dürr and Philipona*, 2004; *Schade et al.*, 2009]. As noted by *Schade et al.* [2009] the underestimation of APCADA, however, cannot be solely explained by undetected cirrus clouds.

3.3. Cloud Type Classification

The performance of the PMOD cloud type classification algorithm was determined using the Payerne training set and the Leave-One-Out Cross-Validation (LOOCV) method. In this method, one single picture from the training set is removed and the algorithm is trained with the remaining data. Then the excluded element, which is independent of the training data, is classified. This is repeated *n* times, where *n* is the number of elements in the training set, such that each element in the training set is used for validation exactly once.

The results of the LOOCV method are given in Table 3. The scores of correctly classified pictures ranged from 89.9 up to 98.5% for cumulonimbus-nimbostratus and cirrus-cirrostratus, respectively, and was only substantially lower for cirrocumulus-altocumulus. Here only 71.4% of the images classified by the observers in the sky camera image as cirrocumulus-altocumulus were classified by the algorithm as this cloud type, while the algorithm classified 15.7% of these images as cumulus. Ten percent of the cirrocumulus-altocumulus images were classified as stratocumulus and the remaining 2.9% were attributed to the other cloud classes. The mean success rate of the algorithm was 91.7%.

The mean success rate for the random test sets decreased significantly and was between 50 and 57% at Zimmerwald, Payerne, and Davos (see Figure 5). The *x* axis of the bar plots denotes the true cloud class as determined by the observers from the sky camera images. The bars represent the relative frequencies of the cloud types classified by the PMOD algorithm for the respective cloud class. For example, 80% of the images from the Payerne test set which were classified by the observers as stratocumulus were also classified as stratocumulus by the algorithm. However, 10% of the stratocumulus images (as classified by the observers) were classified by the algorithm as stratus-altostratus and cumulonimbus-nimbostratus, respectively. While the success rate for cirrus-cirrostratus, stratocumulus, and cloud-free conditions averaged over the three stations Payerne, Zimmerwald, and Davos remained at 61, 62, and 71%, respectively, the mean hit rate for the remaining cloud classes was lower at 43–49%. At Zimmerwald, a frequent misclassification at 70% of the cumulonimbus-nimbostratus class into stratus-altostratus was observed while the algorithm correctly recognized this cloud class in 68% of cases at Payerne.

Due to its altitude, a particular situation occurs at Jungfraujoch. The site is often within clouds, and cloud conditions can change rapidly (see Movie S1 in the supporting information). Therefore, a modification of the cloud classification scheme was necessary in which only cloud-free conditions, cirrus-cirrostratus, cirrocumulus-altocumulus, altostratus, and fog are discriminated. Furthermore, an additional training set

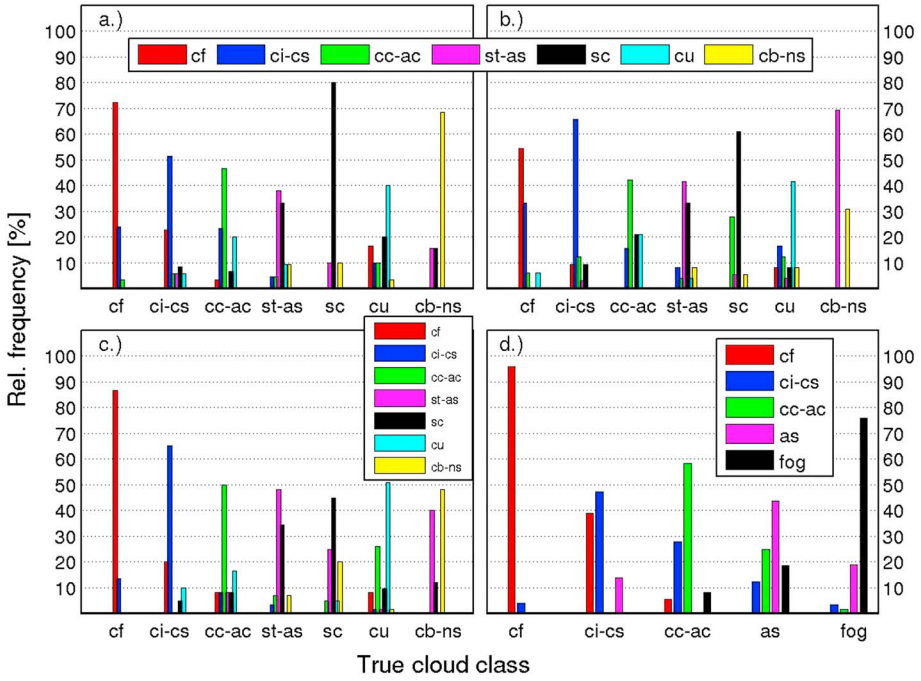

Figure 5. Relative frequencies of correctly and incorrectly classified cloud classes for the test sets of (a) Payerne, (b) Zimmerwald, (c) Davos, and (d) Jungfraujoch. The mean success rate was 50, 55, 57, and 70% for Zimmerwald, Payerne, Davos, and Jungfraujoch, respectively. The Payerne, Zimmerwald, and Davos test sets were classified using the PMOD algorithm trained with the Payerne training set. For Jungfraujoch, the PMOD algorithm was trained using an individual training set consisting of pictures from Jungfraujoch. The sets contain 163, 184, 195, and 204 images for Zimmerwald, Payerne, Jungfraujoch, and Davos, respectively. The images do not necessarily show one cloud class and were randomly selected.

was required to train the algorithm for these particular conditions and the specific camera and hardware characteristics of the MOBOTIX camera. Up to 70% of the Jungfraujoch test set images were correctly classified using this individual training set (see Figure 5d). While cloud-free conditions were correctly recognized in over 95% of cases, the classification of altostratus and cirrus-cirrostratus was more problematic. Indeed, only 44 and 47% of the respective images were correctly classified. The frequent misclassification of cirrus-cirrostratus as cloud free may be explained by the bright pixels near the Sun and/or the poor camera quality. The success rate for cirrucumulus-altocumulus and fog was substantially higher at 58 and 76%, respectively.

4. Discussion

Results from the intercomparisons of total cloud cover indicate that the sky camera overestimates total cloud cover with respect to the other automatic methods, while an underestimation was observed compared to the human observations. Since all automatic techniques underestimate cloudiness compared to the visual observations, it is likely that the human observers at the two study sites have a tendency to overestimate total cloud cover. Contingency tables calculated for all intercomparisons (but not shown here because of conciseness) demonstrate that the overestimation is mainly caused by situations when the observer reported 1 okta and overcast conditions while the automatic methods calculated a cloud-free sky and 7 oktas, respectively. The overestimation by the sky camera with respect to the other automatic methods is due to bright pixels close to the Sun, high solar zenith angles, and/or high turbidity in the atmosphere resulting in a high sky whiteness [*Long*, 2010]. In addition, *Long* [2010] mentioned the intensity range limitations of the detector, i.e., the quality of the camera, which is essential for a correct decision during such atmospheric conditions. Despite the use of an additional underexposed image, the overestimation persists in this study particularly for specific atmospheric conditions. A sample figure from Payerne in winter characterized by a high solar zenith angle and a high aerosol optical depth can be found in the supporting information (Figure S1). The sky camera calculated 2 okta cloudiness despite the fact that no

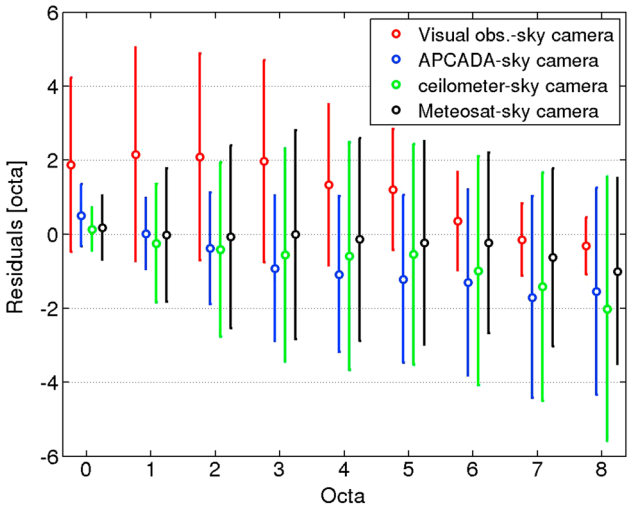

Figure 6. Mean bias (circle) and root mean squared error (corresponding to an uncertainty of approximately 65%, assuming a normal probability distribution) as a function of cloudiness for the Payerne intercomparison. Cloud cover refers to the value calculated using the PMOD algorithm. Mean bias between human observer-sky camera, APCADA-sky camera, ceilometer-sky camera, and Meteosat-sky camera was 0.8 ± 1.9, −0.9 ± 2.2, −1.1 ± 2.8, and −0.5 ± 2.3 oktas, respectively.

cloud was visible which was confirmed by other methods. Cloud detection using a haze correction factor derived from spectral radiation measurements is therefore more effective than the use of an underexposed image for such events [*Ghonima et al.*, 2012; *Shields et al.*, 2013]. Alternatively, other atmospheric parameters such as SZA, specific humidity, (broadband) short- and long-wave radiation may be used to determine such a haze correction factor or sky whiteness index.

The offset between the sky camera and the other techniques is not constant but depends on cloud cover (see Figure 6). The underestimation of the sky camera (and the remaining automatic methods) with respect to the human observer is largest when the sky camera calculates 0–3 oktas. Indeed, the cloudiness reported by the human observer was on average 2 oktas higher, while the bias between the automatic techniques was close to zero for these okta bins. In addition, the uncertainties between the sky camera and the visual observations are considerably higher as indicated by a root mean squared (RMSE) error by up to 3 oktas. For the remaining okta bins, the (positive) offset and the uncertainties between the visual observations and the sky camera decrease with increasing cloudiness. When the sky camera calculates 7 or 8 oktas, the outputs from the sky camera and the human observer are consistent and only a weak overestimation by the sky camera can be on average observed. The remaining automatic techniques, however, tend to underestimate cloudiness when the sky camera and the human observer report and overcast conditions. In addition, the uncertainties between the sky camera and the other automatic methods increase with increasing cloud amount particularly between the sky camera, APCADA and ceilometer. The bias is smallest at 1 okta or less between the sky camera and Meteosat, but the RMSE is fairly high at 2 oktas for all sky conditions except when no clouds are in the sky.

The analysis of the Davos data set (same camera system) yielded similar offsets, while the offsets at Jungfraujoch were slightly different, most likely due to the different camera system used at Jungfraujoch (MOBOTIX). Note that the uncertainties at Jungfraujoch, however, were not larger despite the poorer quality of the MOBOTIX system. These results demonstrate that it will be mandatory to consider the dependencies of the bias on cloudiness instead of applying a constant offset when records of total cloud cover from various methods will be homogenized.

Regarding the cloud type classification, the true cloud class can be reliably determined if a single cloud class occurs in the image. However, if various cloud classes are present in the sky the classification is less reliable as indicated by a mean success rate which can decrease to 50%. A low success rate for a particular cloud class and station is not necessarily solely due to the algorithm but also due to other factors such as the randomness of the selection procedure and/or visual misclassification of the cloud class in the camera image by human observers. In fact, it is more difficult to determine the cloud class in a picture than outside under the sky. To demonstrate the effect of the randomness in the selection procedure we manually generated a second test set for the Payerne site. The mean success rate for this test set was more than 20% higher than for the corresponding automatically generated set (see Table 3) and thus consistent with scores found in similar studies [e.g., *Heinle et al.*, 2010; *Kazantzidis et al.*, 2012]. The classification was significantly better for all cloud classes except for stratocumulus when using the PMOD algorithm. The success rate of the sky analyzer was even slightly higher at 83.1% compared to the PMOD algorithm. All cumulonimbus-nimbostratus clouds were correctly classified using the sky analyzer. Problematic here was only the

classification of the stratus-altostratus class where only 53.3% of the images were correctly recognized while 10.0 and 36.7% were misclassified as cirrocumuls-altocumulus and cumulonimbus-nimbostratus, respectively. A similar test set was also produced for Zimmerwald yielding the same results. This implies that the algorithm, when trained at a particular site, can be applied at any different site as long as the site characteristics including atmospheric conditions of the training site are representative of the target site and the same camera system is used. However, if this is not the case as, for instance, at Jungfraujoch, the algorithm must be trained to the specific conditions and the camera system of the respective site. Therefore, an individual training set is necessary.

5. Conclusions

We have established a hemispherical sky camera network comprising four sites in Switzerland for observations of total cloud cover and cloud type classification. Sky cameras have the strong advantage that they image the whole hemisphere and therefore allow the instantaneous total cloud cover to be reliably calculated on the basis of highly resolved pixels and hence in percent coverage of the sky. We compared total cloud cover from the sky camera to the corresponding outputs derived from various techniques including ceilometer, Meteosat, observations of long-wave radiation, and visual observations. Cloudiness from the sky camera was within ± 1 okta for 65–85% of cases with respect to the other techniques. The sky camera overestimates cloudiness with respect to the other automatic methods particularly when the sky whiteness is high due to haze. All automatic techniques, however, tend to underestimate total cloud cover compared to the visual observations which were available at two sites. Thus, the sky camera is closest to the visual observer. The results demonstrate that the replacement of visual observations by automatic methods would introduce a bias in the highly valuable long-term synoptic time series at these sites. In addition, we showed that a possible homogenization of cloud cover records derived from various observational techniques cannot be conducted using a constant offset but requires a correction function instead which depends on cloud cover and used hardware and hence needs to be determined for each site individually.

Besides the observation of total cloud cover, sky cameras offer a variety of other applications such as cloud type classification, determination of cloud base, and forecasting of cloud motion and solar irradiance. We studied cloud type classification at four sites using the *k*-nearest neighborhood classifier in combination with a total of 12 features including spectral and textural features, cloud cover, and a radiative feature. Over 90% of the images were correctly classified when the algorithm was trained to be site specific, and only one cloud class occurred in the image. However, when the algorithm was applied to the remaining sites and/or multiple cloud classes occurred in the image, the mean success rate decreased substantially to 50–80% depending on the randomness of the image selection procedure and the visual misclassification of the clouds in the sky camera image by the observers. Moreover, the current cloud type algorithm is sensitive to site and camera characteristics (e.g., site altitude and camera settings) and site-specific atmospheric conditions. The algorithm can be trained at one site and applied to different locations as long as the cloud classes are representative and the same camera system is used. Otherwise the algorithm might be revised and trained to the site-specific conditions and camera system using an individual training set. Consequently, the development of a uniform and site-independent cloud cover and cloud type algorithm is in this context not a constructive goal.

Hemispherical sky cameras are a powerful tool to precisely detect clouds and they are currently the only automatic technique to conduct cloud type classification. However, different cameras and image processing algorithms are in use resulting in uncertainties which we estimate to be about 10 % based on a comparison of two different image processing algorithms conducted in this study. In fact, these issues have also been addressed in a COST-ES1002(http://www.wire1002.ch/) international workshop on sky cameras recently held in Patras/Greece(http://www.sky-camera-workshop.info/). There is consensus that it would be highly valuable to establish a benchmark data set of cloud observations (total cloud cover and cloud type) from ground and satellite-based retrievals in order to study the performance of the various methods, to assess their uncertainties and to evaluate possible optimization, standardization, and/or homogenization procedures. The overall goal of such an action would be the development of a unique ground-based observing system dedicated to an accurate monitoring of total cloud cover, cloud type, and the variations in order to improve the validation of satellite-based cloud retrievals and climate model outputs, and therefore to reduce the persisting uncertainties related to clouds and climate change.

A certain drawback of most hemispherical sky cameras which are in use for the visible spectral range is their limitation to daytime. For nighttime operation, either highly sensitive cameras in the visible range such as the day/night whole sky imagers or cameras operating in the thermal infrared are necessary. In a follow-up project, we are currently developing a thermal infrared all-sky cloud imager in order to observe clouds in combination with visible sky cameras during day and night.

Acknowledgments

This research was carried out in the frame of the project Cloud climatology and Surface radiative forcing over Switzerland (CLASS) financed by MeteoSwiss. Data from all-sky cameras are available via email (julian.groebner@pmodwrc.ch) upon request. Modification of the ventilation unit design for the MOBOTIX cameras was performed by D. Bühlmann and M. Spescha from PMOD/WRC. We acknowledge Jean-Christian Zill and Clement Chevre from MeteoSwiss, and Andres Luder and Adrian Jenk from the Institute of Applied Physics for installation and image acquisition at the respective sites. Gonzague Romanens from MeteoSwiss provided the ceilometer data. P. Tzoumanikas and A. Kazantzidis acknowledge (a) the European Commission for funding the project DNICast (www.dnicast-project.net), grant agreement: 608623, (b) the General Secretariat for Research and Technology, Greek Ministry of Education, Lifelong Learning and Religious Affairs for funding the project ÂŽHellenic Network of Solar Energy (www.helionet.gr, 09SYN-32-778). MSG SEVIRI based Cloudiness was provided by MeteoSwiss as part of their engagement in the EUMETSAT Satellite Application Facility on Climate Monitoring (CM SAF) project. Finally, we highly appreciate the fruitful comments of three anonymous reviewers who helped to improve the manuscript substantially.

References

Boers, R., M. J. de Haij, W. M. F. Wauben, H. K. Baltink, L. H. van Ulft, M. Savenije, and C. N. Long (2010), Optimized fractional cloudiness determination from five ground-based remote sensing techniques, *J. Geophys. Res.*, *115*, D24116, doi:10.1029/2010JD014661.

Boucher, O., et al. (2013), Clouds and Aerosols, in *Climate Change 2013: The Physical Science Basis. Contribution of Working Group I to the Fifth Assessment Report of the Intergovernmental Panel on Climate Change*, edited by T. F. Stocker et al., Cambridge Univ. Press, Cambridge, U. K., and New York.

Dai, A., T. R. Karl, B. Sun, and K. E. Trenberth (2006), Recent trends in cloudiness over the United States: A tale of monitoring inadequacies, *Bull. Am. Meteorol. Soc.*, *87*, 597–606, doi:10.1175/BAMS-87-5-597.

Dürr, B., and R. Philipona (2004), Automatic cloud amount detection by surface longwave downward radiation measurements, *J. Geophys. Res.*, *109*, D05201, doi:10.1029/2003JD004182.

Eliasson (2005), Ceilometer cbme80 user's guide.

Feister, U., and J. Shields (2005), Cloud and radiance measurements with the VIS/NIR daylight whole sky imager at Lindenberg (Germany), *Meteorol. Z.*, *14*, 627–639, doi:10.1127/0941-2948/2005/0066.

Ghonima, M. S., B. Urquhart, C. W. Chow, J. E. Shields, A. Cazorla, and J. Kleissl (2012), A method for cloud detection and opacity classification based on ground based sky imagery, *Atmos. Meas. Tech.*, *5*, 2881–2892, doi:10.5194/amt-5-2881-2012.

Gröbner, J., S. Wacker, L. Vuilleumier, and N. Kämpfer (2009), Effective atmospheric boundary layer temperature from longwave radiation measurements, *J. Geophys. Res.*, *114*, D19116, doi:10.1029/2009JD012274.

Heinle, A., A. Macke, and A. Srivastav (2010), Automatic cloud classification of whole sky images, *Atmos. Meas. Tech.*, *3*, 557–567.

Johnson, R. W., S. Hering, and J. E. Shields (1989), Automated visibility and cloud cover measurements with a solid-state imaging system, *Tech. Rep.*, Marine Physical Laboratory, Scripps Institution of Oceanography, Univ. of California, San Diego, Calif.

Kalisch, J., and A. Macke (2008), Estimation of the total cloud cover with high temporal resolution and parametrization of short-term fluctuations of sea surface insolation, *Meteorol. Z.*, *17*, 603–611, doi:10.1127/0941-2948/2008/0321.

Karlson, K.-G., E. Wolters, P. Albert, A. Tetzlaff, R. Roebeling, W. Thomas, and S. Johnston (2005), Validation of CM-SAF cloud products using MSG/SEVIRI data, *Sci. Rep. ORR V2*, Offenbach.

Kazantzidis, A., P. Tzoumanikas, A. F. Bais, S. Fotopoulos, and G. Economou (2012), Cloud detection and classification with the use of whole-sky ground-based images, *Atmos. Res.*, *113*, 80–88, doi:10.1016/j.atmosres.2012.05.005.

Kreuter, A., M. Zangerl, M. Schwarzmann, and M. Blumthaler (2009), All-sky imaging: A simple, versatile system for atmospheric research, *Appl. Opt.*, *48*, 1091–1097, doi:10.1364/AO.48.001091.

Long, C. N. (2010), Correcting for circumsolar and near-horizon errors in sky cover retrievals from sky images, *Open Atmos. Sci. J.*, *4*, 45–52, doi:10.2174/1874282301004010045.

Long, C. N., and J. J. DeLuisi (1998), Development of an automated hemispheric sky imager for cloud fraction retrievals, in *Proceedings of the 10th Symposium on Meteorological Observations and Instrumentation*, Am. Meteorol. Soc., Phoenix, Ariz.

Long, C. N., J. M. Sabburg, J. Calbó, and D. Pagès (2006), Retrieving cloud characteristics from ground-based daytime color all-sky images, *J. Atmos. Oceanic Technol.*, *23*, 633–652, doi:10.1175/JTECH1875.1.

National Oceanic and Atmospheric Administration (1998), Automated surface observing system.

Norris, J. R., and A. Slingo (2009), 2 trends in observed cloudiness and Earth's radiation budget: What do we not know and what do we need to know?, in *Clouds in the Perturbed Climate System*, edited by J. Heintzenberg and R. J. Charlson, pp. 17–36, MIT Press, Cambridge, Mass.

Ohmura, A., et al. (1998), Baseline Surface Radiation Network (BSRN/WCRP): New precision radiometry for climate research, *Bull. Am. Meteorol. Soc.*, *79*, 2115–2136, doi:10.1175/1520-0477(1998)079<2115:BSRNBW>2.0.CO;2.

Quesada-Ruiz, S., Y. Chu, J. Tovar-Pescador, H. T. C. Pedro, and C. F. M. Coimbra (2014), Cloud-tracking methodology for intra-hour DNI forecasting, *Sol. Energy*, *102*, 267–275, doi:10.1016/j.solener.2014.01.030.

Schade, N. H., A. Macke, H. Sandmann, and C. Stick (2009), Total and partial cloud amount detection during summer 2005 at Westerland (Sylt, Germany), *Atmos. Chem. Phys.*, *9*, 1143–1150.

Shields, J. E., R. W. Johnson, and T. L. Koehler (1990), Whole sky imager, Proceedings of the Cloud Impacts on DOD Operations and Systems, 1989/1990 Conference Science and Technology Corporation, pp. 123-128.

Shields, J. E., R. W. Johnson, M. E. Karr, A. R. Burden, and J. G. Baker (2003), Daylight visible/NIR whole-sky imagers for cloud and radiance monitoring in support of UV research programs, in *Ultraviolet Ground- and Space-based Measurements, Models, and Effects III, Society of Photo-Optical Instrumentation Engineers (SPIE) Conference Series*, vol. 5156, edited by J. R. Slusser, J. R. Herman, and W. Gao, pp. 155–166, Bellingham, Wash., doi:10.1117/12.509062.

Shields, J. E., M. E. Karr, R. W. Johnson, and A. R. Burden (2013), Day/night whole sky imagers for 24-h cloud and sky assessment: History and overview, *Appl. Opt.*, *52*, 1605–1616, doi:10.1364/AO.52.001605.

Stöckli, R. (2013), The heliomont surface solar radiation processing, *Sci. Rep. 93*, MeteoSwiss, 122 pp., Zürich, Switzerland.

Wacker, S., J. Gröbner, and L. Vuilleumier (2014), A method to calculate cloud-free long-wave irradiance at the surface based on radiative transfer modeling and temperature lapse rate estimates, *Theor. Appl. Climatol.*, *115*, 551–561, doi:10.1007/s00704-013-0901-5.

Yang, H., B. Kurtz, D. Nguyen, B. Urquhart, C. W. Chow, M. Ghonima, and J. Kleissl (2014), Solar irradiance forecasting using a ground-based sky imager developed at UC San Diego, *Sol. Energy*, *103*, 502–524, doi:10.1016/j.solener.2014.02.044.